



Coronal Mass Ejections (CMEs) and their geo-effectiveness during Solar Cycles 23 and 24: a comparative analysis of observational properties

¹Priyank Srivastava, ²A.K. Singh

¹Research Scholar, ²Professor, University of Lucknow

¹Department of Physics,

¹University of Lucknow, Lucknow, India

Abstract: One of the most influential solar transients, coronal mass ejections (CMEs) play a decisive role in dealing with solar dynamics. CMEs are the main agents responsible for spatial weather fluctuations and related phenomena. The geo-effectiveness of the CMEs has a significant impact on the terrestrial climate. Owing to the diversity of shapes and the difficulty of the progression of time, the detection and calculation of CMEs remain challenging. As a result, looking at the feasibility of the variable, we analyzed the regular fluctuations of the total, northern and southern components of sunspot numbers observed between 1996-2020 and compared the solar activity trend for solar cycles 23 and 24. We deduced that solar activity was lower in solar cycle 24 than in cycle 23. We have also examined some observational properties such as the central positioning angle (CPA) and the measuring positioning angle (MPA) of all observed CMEs, angular width, variations in angular width with CMEs linear speed, variations of linear speed, acceleration, variations in the linear speed with acceleration, kinetic energy and ejected mass for observed CMEs during solar cycle 23 and 24. Based on these analyses, we inferred that while the number of CMEs observed in the 24th solar cycle (16680) was higher relative to CMEs observed during the 23rd solar cycle (13640), the solar activity decreased in cycle 24 and this could be correlated with the reduced geo-effectiveness of CMEs observed during cycle 24. The intensity of the flare in optical or X-rays does not accurately predict the intensity of the resulting geomagnetic activity. C and M class flares can be associated with intense storms (Dst <-100 nT). The initial speed of CMEs and geomagnetic activity was found to have a moderate and negative Pearson's correlation coefficient of 0.66. This correlation suggests that the prediction of geo-effectiveness is associated with the initial speed of halo CMEs. Thus, based on the number of sunspots and the study of the observational properties of CMEs and their occurrence as well as geo-effectiveness; we concluded that the solar cycle 24 was weakly active in contrast with the solar cycle 23, and also that there was a diminishing pattern in solar activity.

Keywords - Solar cycles; Solar activity; Sunspot numbers; Coronal mass ejections; Geomagnetic Storms

1. INTRODUCTION

Coronal Mass Ejections are a significant solar violent event that hurls enormous amounts of magnetic flux and plasma out of the solar atmosphere, with the potential to have repercussions on the heliosphere, interplanetary space, and Earth's atmosphere (Howard et al. 1982; Webb and Howard 1994, 2012; Lamy et al. 2019). These are the most striking events associated with the dynamic Sun and the primary aspect of space weather that further affect the Sun-Earth system (Pevtsov & Canfield 2001; Gopalswamy et al. 2001; Singh & Singh 2003; Singh et al. 2010, 2014). CMEs are the fundamental component that demonstrates how magnetic energy has evolved, released, and deposited in magnetic flux systems in solar and coronal physics (Fry et al. 2003; Singh et al. 2010; Lamy et al. 2019). CMEs provide pathways for the separation from the Sun of an enormous amount of magnetic flux and helical flux, which forms the basis for another solar cycle. CMEs play an important role in the solar dynamo by ejected magnetic helicity (Low 2001; Webb & Howard 2012).

CMEs generate heliospheric disruptions that accelerate electrons and protons, as shown by radio bursts and solar energetic particles in the context of interplanetary space physics (Xapsos et al. 1999; Singh & Singh 2003; Giamini et al. 2020). Near the solar maximum, CMEs also contribute to solar wind mass flux (Webb & Howard 1994; Lamy et al. 2017). In terms of planetary physics, CMEs affect the magnetosphere, causing magnetic storms that intensify ring currents and eventually cause adverse effects on Earth by disrupting power grids, telecommunications infrastructures, and artificial satellites by altering their trajectories (Singh & Singh 2003; Richardson & Cane 2004; Taktakishvili et al. 2009; Singh et al. 2018).

Knowledge of CMEs associated with solar surface activities, as well as with the Earth, has significant importance since the method of initiating CMEs would raise understanding of the physical link between the solar magnetic field and its activity (Singh et al. 2010). Subramanian & Dere (2001) analyzed coronal mass ejections detected between January 1996 and May 1998 and concluded that approximately 41% of CMEs were related with active regions (ARs) and occurred without prominence eruptions, 44% of CMEs observed were associated with eruptions with active region prominence, while 15% of CMEs observed were associated with quiescent prominence. In their study of CMEs in the years 1997 to 2001, Zhou et al. (2003) observed that about

88% of CMEs were associated with solar flares and 94% were associated with eruptions of prominence and 79% of CME events were associated with ARs and 21% originated outside of ARs. There's some evidence that solar dynamic processes owing to horizontal surface mobility of magnetic flux persist well into solar cycle decline, as Jang et al. (2016) hypothesized. In recent years, remote sensing devices, in-situ data, and certain models have been utilized to explain the source mechanism, propagation, and absence of shock associated with the CMEs (Nieves-Chinchilla et al. 2020; Giacalone et al. 2020).

In specific, Earth-directed CMEs have more significance because they trigger geomagnetic disruptions and may also cause geomagnetic storms. These CMEs are generally categorized as halo CMEs (Howard et al. 1982; Yurchyshyn et al. 2007; Singh et al. 2014, 2018). A fast halo CME, which takes place near the middle of the Earth-facing solar disc, contributes to an intense magnetic field in the south which produces a powerful geomagnetic storm (Pevtsov & Canfield 2001; Kim et al. 2010; Anastasiadis et al. 2019). An Earth-directed CME's initial propagation speed can be precisely measured, providing information on the severity of the geomagnetic storm that preceded it and its occurrence time. To estimate the speed of the CME, several models and approaches have been utilized (Moon et al. 2002; Qiu and Yurchyshyn 2005; Wang and Zhang 2008; Fainshtein et al. 2012; Adam et al., 2019).

According to the number of sunspots (SSNs), solar cycle 24 has been very weak and also the least since the dawn of the space era (Singh & Bhargawa 2017, 2019). Many researchers have predicted that the diminishing pattern of solar activity in the 24th solar cycle could lead to a global minimum in the future (Zolotova & Ponyavin 2014; Padmanabhan et al. 2015; Singh & Bhargawa 2019). On the other hand, the rate of CMEs occurrence has not diminished as much, which is not fully understood (Petrie 2013; Wang & Colaninno 2013; Gopalswamy et al. 2015). The space weather events in cycle 24 have been extremely mild even with the high occurrence rate of CMEs this may be connected with the geo-effectiveness of the CMEs observed (Werner et al. 2019).

We investigated the regular fluctuations in the total number of sunspots for both the cycles and the variability in the sunspot number in the north and south, various observational properties such as the central positioning angle and the measuring positioning angle of all observed CMEs, angular width, angular width variations with linear speed, linear speed variations, acceleration, linear speed variations with acceleration, mass expelled and kinetic energy of the observed ejections during solar cycles 23 & 24 and provided comparative study. Section 1 includes a short introduction to the characteristics of coronal mass ejections. Properties of CMEs and information about data sources are provided in section 2. Section 3 discussed the solar activity and the rate of CMEs. The link between Coronal Mass Ejections and geomagnetic storms, as well as some of SC 23's major storms, are discussed in section 4. Results and discussion are described in section 5 and finally, conclusions are presented in section 6.

2. PROPERTIES OF CMES AND DATA SOURCES

Closed-field regions around the Sun where magnetic free energy is concentrated and unexpectedly emitted in the form of CMEs are known as active regions (Green et al. 2018). Height-time measurement is an important aspect that plays a role in the estimation of other observable properties of ejections. The angle of the measuring position is the angle at which the height-time measurements are made, whereas the central position angle is the center position relative to the extreme edges of the mass ejections in the sky plane. Based on CPA values, CMEs can be distinguished simultaneously by their forms. Ideally, due to the non-radial movement of several CMEs, central and measuring PAs must have the same value, but due to the non-radial movement of some CMEs, both can differ, as in the case of halo (360°) where there is no CPA value but the fastest moving part of the CME's leading edge has an MPA. The linear speed is determined by the straight-line fitting of the height-time measurements of the eruption. Depending on their speed, coronal mass ejections might be divided into two categories: the slow and the fast ones. Slow CMEs are associated with eruptive prominence, while fast CMEs originate in solar-active areas. In a few cases, fast CMEs travel at a constant speed, whereas slow ones show accelerated patterns. Subsequently, CMEs are further divided into two groups as gradual CMEs and impulsive CMEs. Gradual CMEs were associated with erupting prominences and speeds within 400-600km/s while impulsive CMEs had speeds ≥ 750 km/s and were associated with solar flares.

The data used in the present study for statistical analysis are obtained from the catalogue of SOHO's website (https://cdaw.gsfc.nasa.gov/CME_list/catalog_description.htm) as the LASCO is observing CMEs continuously since January 1996 (since the start of solar cycle 23). We have analysed all the ejection events (CMEs) observed during solar cycles 23 and 24. In a few cases, there are gaps in the pictorial representations (graphs) but this is only due to the unavailability/missing of data. Table 1 has listed an overview of the comparison between the observed parameters of the CMEs which indicates the declining trend of solar activity during cycle 24. To establish the correlation between the observational properties, we have used the ordinary least square and Pearson's correlation method. For studying the variations in the sunspot numbers, we have evaluated sunspot number data from the World Data Centre SILSO from January 1996 to June 2020. The total number of observations was 8887, and we have also derived the daily total, north and south sunspot numbers. The Dst indices were collected from the World Data Center geomagnetic activity web page (<http://swdcwww.kugi.kyoto-u.ac.jp>).

3. SOLAR ACTIVITY AND CME RATE

The only confrontational route for analysing the prolonged evolution of the solar cycle is the time series of sunspot numbers and is widely used in various fields, especially in Solar Physics. It offers crucial information on multiple observational properties as their higher and lower numbers are closely related to solar activity (Singh & Bhargawa 2017, 2019). Fig. 1(a,b) represents the differences in the daily average SSN and the daily north/south SSN in the years 1996-2020 (solar cycles 23 & 24). Fig. 1 demonstrates that the solar cycle 23 sunspot number was greater than the solar cycle 24 count, indicating that solar activity was stronger during the solar cycle 23 compared to the sunspot count during the solar cycle 24. In addition, the graph shows a time series plot of the north/south sunspot counts observed during solar cycles 23 and 24. In solar cycle 23, the mean value of sunspots in the north was ~36.97 and ~41.84 in the south, whereas in solar cycle 24, the mean value of sunspots in the north was ~25.11 and ~23.03 in the south. These differences in the north and the south sunspot numbers are known as N-S asymmetry concerning the equator and this asymmetry is always present in the solar cycles during the rising or declining phases. Studies of the N-S asymmetry and its link to solar activity have been conducted by a variety of researchers (Waldmeier 1971; Verma 1993; Ballester et al. 2005). Based on the mean values observed in the present study, we can conclude that solar cycle 23 was south dominant and solar cycle 24 was north dominant. The mean of total sunspot numbers in solar cycles 23 and 24 were ~78.82 and ~48.15. This difference in

the sunspot numbers, clearly suggests that solar cycle 24 is magnetically weaker than solar cycle 23. Fig. 2 illustrates the rate of CMEs in solar cycles 23 and 24, with the ejection rate in the latter being greater than the number of ejections in the former.

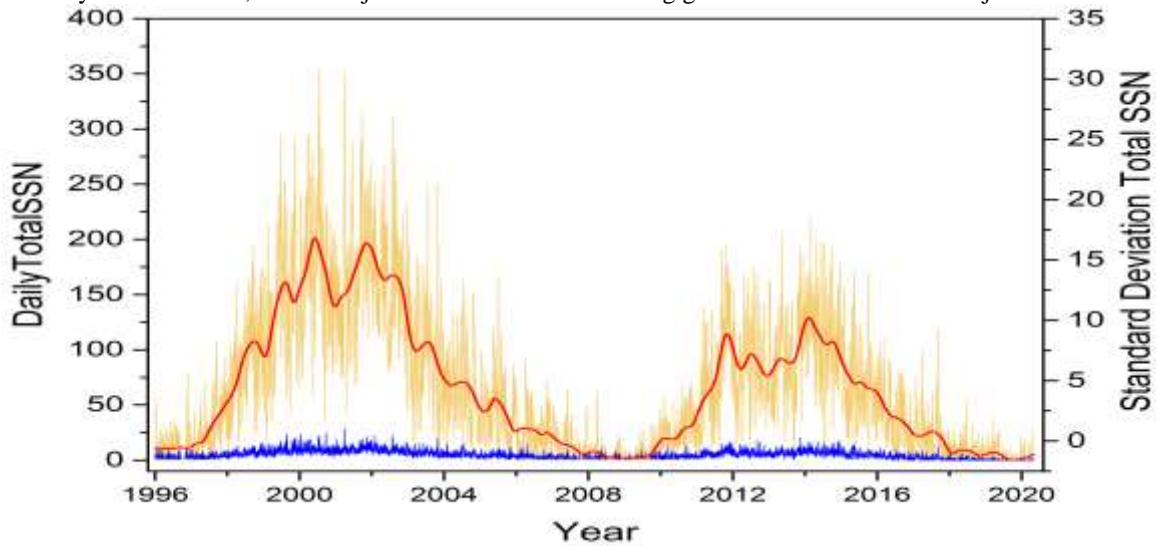


Figure. 1(a) Time series plot for daily total sunspot numbers observed during solar cycles 23 (1996-2008) and 24 (2008-2020).

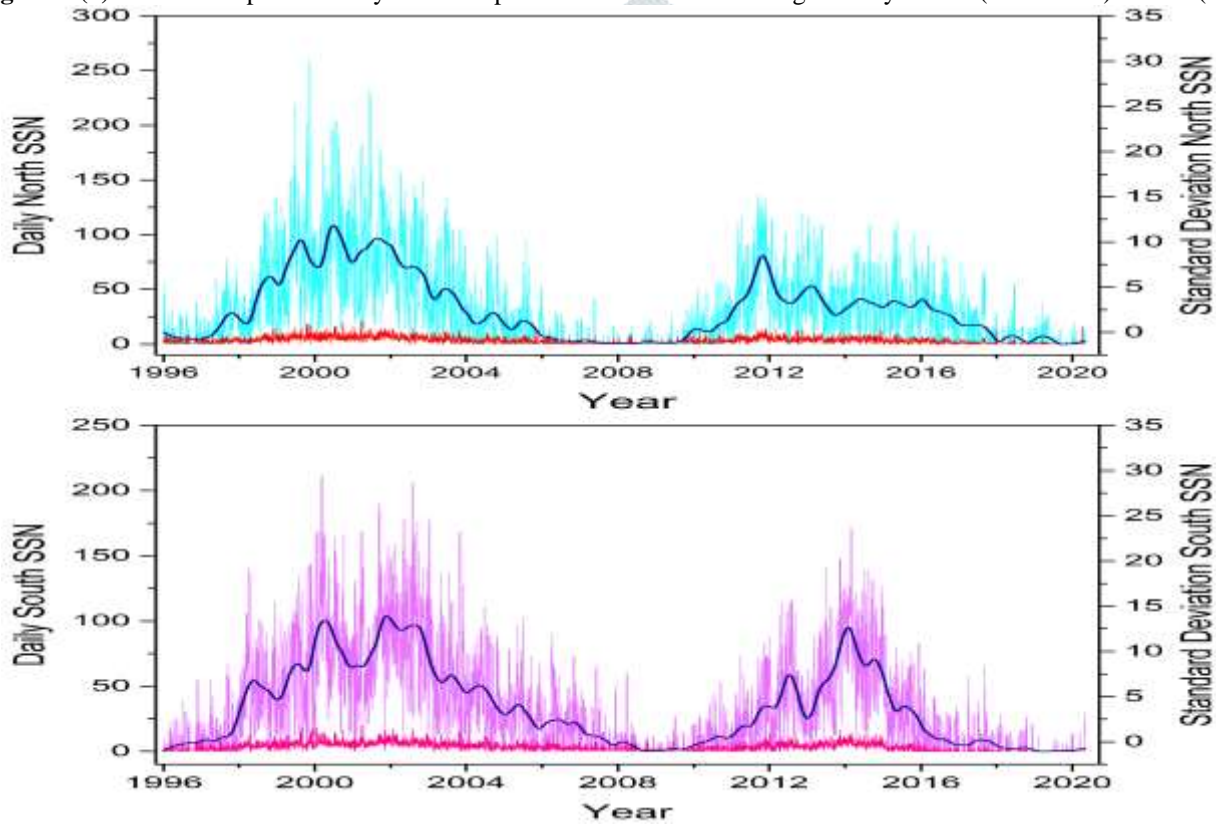


Figure. 1(b). Time series plot for daily north and south sunspot numbers observed during solar cycles 23 (1996-2008) and 24 (2008-2020).

In photospheric magnetograms, CMEs originated in closed magnetic field regions that appear as bipolar or multipolar. These magnetic regions containing sunspots represent good historical indicators for solar activity. Usually, there are positive correlations between sunspot numbers and CMEs rate (Webb & Howard 1994; Gopalswamy et al. 2010) but is not absolute because CMEs originate from non-spot regions also. The importance of the solar cycle 24 lies in the fact that it is the weakest in the space era and has provided mild effects on the space weather events related to solar origin (Gopalswamy et al. 2014). Though in proportion to the sunspot numbers which declined by about 40% in solar cycle 24, the CMEs activity has not decreased (Gopalswamy et al. 2015; Howard & Vourlidas 2018).

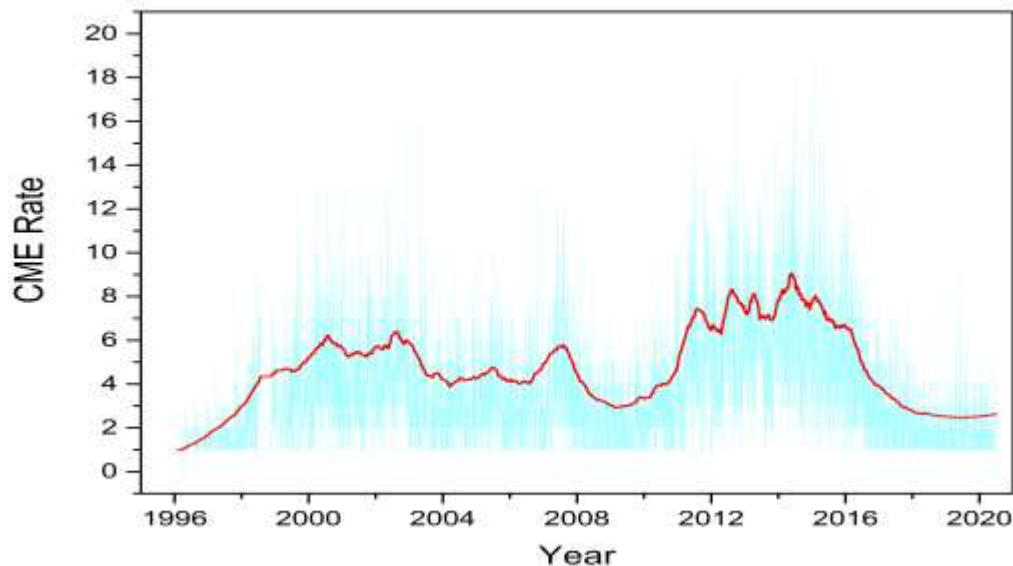


Figure. 2. Time series plot of CME rate for solar cycle 23 and 24 using Savitzky-Golay method for smoothing.

4. CORONAL MASS EJECTIONS (CMEs) AND GEOMAGNETIC STORMS

The geomagnetic storm is one of the immediate repercussions of CMEs entering the magnetosphere of the Earth. The ecliptic component (B_z) of the IMF is the key link between a geomagnetic storm and a CME (Gopalswamy 2009). The cause of geomagnetic storms is the re-joining of the CME field and the magnetic field of the Earth when B_z is pointing south (Gopalswamy 2008). The B_z component in the quiescent solar wind is insignificant, but CMEs contain B_z due to their flux rope structure. The compressed sheath field between the flux rope and the shock can also contain B_z since fast CMEs generate shocks (Manchester IV et al. 2005). This means that B_z can arise from the flux rope and sheath. The Dst index (in nT) is a measure of the strength of geomagnetic storms and is calculated from the horizontal component of the Earth's magnetic field recorded at several equatorial sites (Sabaka et al. 2004). Most major storms are triggered by CMEs and have $Dst \leq -100$ nT (Zhang et al. 2007). "Superstorms," or storms with Dst intensities of less than -250 nT, may be caused by magnetic clouds (Echer et al. 2008). Storms of this intensity are not caused by sheaths or CIRs. Because the slow solar wind magnetic field is between 5 and 7 nT, Kennel et al. (1985) demonstrated that fast shocks can compress the magnetic field by a factor of around 4, regardless of the shock Mach number. Thus, the maximum field strengths of interplanetary sheath fields and CIR magnetic fields should be in the range of 20 to 35 nT. Magnetic cloud fields, on the other hand, have ranged from 50 to 60 nT, and in extreme circumstances, up to 100 nT. As a result, even if the sheath and CIR magnetic fields are completely southern, they are insignificant in contrast to magnetic cloud fields (Gopalswamy et al. 2008).

4.1 High-speed CMEs, associated class of solar flare and geomagnetic storm intensity

Interplanetary and geomagnetic activity is now widely accepted to be primarily driven by CMEs (Srivastava & Venkatakrishnan 2002). Since CMEs originate from the solar surface, they must be tracked through the interplanetary medium until they reach Earth to demonstrate a physical link between solar origin and geomagnetic effect. To solve the underlying issues associated with geomagnetic storm prediction, one must investigate halo CMEs. Halo CMEs appear as expanding, circular brightening's encircling the coronagraph's occulter and can be directed either towards or away from the Earth. However, not all halo CMEs create geoeffective IP shocks and sheaths. In this section, we have examined the most intense CMEs of solar cycles 23 and 24 and the consequent geomagnetic storms with $Dst \leq -300$. We analysed these two occurrences to determine the exact parameters that led to the strongest geomagnetic storms of the two previous solar cycles.

4.1.1 The CME of July 14, 2000

The SOHO/LASCO imagery indicated a full halo, Earth-directed CME at 10: 54 UT on July 14, 2000 (14/10:54 UT) with a linear speed of 1674 km/s. This CME was linked with an X5/3b x-ray event, which occurred at 14/10:24 UT and was produced by region 9077 (N18W09). Region 9077 also produced an M3/1n at 14/13:44 UT. Sunspot region 9077 was part of the FK C (β - γ - δ) group. As a result of this disturbance, the Earth observed it approximately 27 hours after the Sun. The geomagnetic field was unsettled to severe storm levels on July 15. The sudden storm commencement began at 15/14:40 UT. This storm was related to the X5/3b event on 14 July and the Dst index valued at -301 nT. The energy channel $E > 10$ MeV proton event had reached a peak of 24000 pfu's at 15/12:30 UT and $E > 100$ MeV proton event, that began 14/10:40 UT, peaked at 410 pfu at 14/16:20 UT and ended at 16/04:00 UT. During the storm period, a moderate (8.2 percent) Forbush decrease was observed on the Thule, Greenland neutron monitor.

4.1.2 The CME of March 28, 2001

On March 28, 2001, the solar activity was moderate. Region 9393 (N13E00) produced the most activity with four M-class events during the day. The first was an M1/Sf at 28/01:58 UT, the second was an M1/Sn at 28/09:47, the third was an M4/Sf at

28/12:40 UT and the fourth was an M1/f at 28/19:09 UT. Regions 9403 (S13E36) and 9397 (S09E19) produced upper C-class level events. The continuously growing region 9393 covered an area of over 2200 millionths in white light. In addition, the region maintained a highly complex (β - γ - δ) magnetic configuration. On March 28, 2001, LASCO observed a full halo (360°) CME associated with an M4/Sf flare event. At 12:50 UT, the CME was visible in LASCO-C2 as a bright narrow front over the NW limb. Before decelerating, the CME expanded at $v > 1600$ km/s and about 25R, the speed decreased to 519 km/s.

At around 00:15 UT on March 31, 2001, a strong IP shock associated with the March 29, 2001 halo CME arrived at the SOHO. Currently, the geomagnetic field is experiencing severe storm conditions. This occurred at 31/00:23 UTC and reached Earth's magnetic field at 31/00:51 UTC and associated with X1/1n flare event. After that, the storm intensified and reached its maximum intensity ($Dst = -387$) at 31/09:00 UT on the 31st. It's been going on since the early morning hours of UT. There have been reports of dynamic auroral displays across the United States, with Arizona, west Texas, and California reporting the most. 29/10:00 UTC was the start time of the solar proton event, which was declared over at 01/06:30 UTC.

4.1.3 The CME of October 28, 2003

X17/4b proton flare peaking at 28/11:10 UTC on October 28, 2003, in region 486 (S17E04) was one of the largest flares of this solar cycle. On SOHO/LASCO imagery, a full halo CME with a very fast (nearly 2000 km/s) earthward-directed speed was observed. In solar cycle 23, it has become one of the largest and most complicated active areas on the sun and that region is a (β - γ - δ) group with an area of over 2100 millionths of white light coverage. As it approaches the west limb, Region 484 (N03W68) retains its size and complexity. A low-level M flare occurred at 28/16:13 UT, along with some C-class activity. Region 488 (N08W04) continues to expand rapidly, surpassing 800 millionths of coverage in a (β - γ - δ) configuration. Throughout the period, there was a lot of C-class flare activity in this area. Today, the new region 493 (N09E05) was assigned a number.

There was intense storming in the geomagnetic field on October 29 and the Dst index value was -353nT. CME from the X17/4b flare hit the Earth's magnetic field around 29/06:13 UTC on June 29th. On the Boulder magnetometer, the impulse was measured at 140 nT. In the 29/06:00 UT – 09:00 UT timeframe, a strong southward IMF Bz initiated severe (K9) storming at middle and high latitudes. From 29/09:00 to 18:00 UT, mostly northward Bz occurred; however, major to severe storming persisted. At around 1800Z, the Bz took a sharp southward turn, bringing the period to a close with K8-9 severe storming. Forbush has been reduced by more than 20 percent in recent years. As a result of the X17 flare's large proton event and GLE, these events are already reducing. There were 29,500 pfu in the energy channel $E > 10$ MeV proton event on 29/06:15UT, making it the cycle's second greatest $E > 10$ MeV proton event (second only to the 31,700 pfu proton event in November 2001). There was an $E > 100$ MeV proton event that started at 28/11:45 UT and reached its peak of 186 pfu at 29/00:15 UT.

4.1.4 The CME of October 29, 2003

Solar activity was also high on this day. Region 486 (S17W09) produced an X10 flare at 29/20:49 UT and this strong flare was existential at the end of the day. At 29/05:11 UT, Region 486 also produced an M3. It is the biggest sunspot group in solar cycle 23 with a white light coverage of 2600 millionths of an area. Continuously expanding, it has a complicated (β - γ - δ) structure, and it's still growing. Region 488 (N08W18) is also a large, complex active region, with a (β - γ - δ) configuration that now exceeds 1200 millionths Observations in this region included C-class activity and low M-class flares. As it revolves around the west limb, the extremely large and active Region 484 (N01W81) is rather quiet.

The geomagnetic field was dominated by minor to severe storms. The powerful geomagnetic storm that began at 29/06:11 UT lasted for the first half of this period. From 29/21:00 to 30/03:00 UT, severe (K8-9) levels were observed. The onset of another severe geomagnetic storm was preceded by a brief "quiet" (Kp 5-6) activity. The very fast CME from the X10 flare, which peaked at 29/20:49 UT, impacted the magnetic field at around 30/16:00 UT, completing a remarkable 19-hour transit from Sun to Earth. Since the start of this severe storm, the geosynchronous satellites GOES-10, 11, and 12 have undergone magnetopause crossings and have remained outside the magnetopause for much of the period. In the -15 to -30nT range, an IMF Bz that continues to go south suggests a significant response. A Forbush decrease of about 20% is still in progress. A fresh rush of high-energy protons occurred after the X-10 flare, adding to the previous $E > 10$ MeV and $E > 100$ MeV proton occurrences from the 28th X17 flare. At $E > 100$ MeV, this augmentation attained 110 pfu (29/23:10 UT) and 3300 pfu (30/19:35 UT) at $E > 10$ MeV.

4.1.5 The CME of November 18, 2003

On November 18, 2003, solar activity was moderate. Several M-class flares were observed in Region 501 (N03E09). The most notable flares were a pair of M3/2n flares with peak fluxes at 18/07:52 UT and 18/08:31 UT. A filament channel erupted to the south and west of this region in continuity with the initial flare. As a consequence of a series of complicated events, a full halo CME (initial speed of 1660 km/s) was depicted by LASCO. Over the last 24 hours, this region has grown and evolved into a (β - γ - δ) magnetic complex. During this period, the biggest flare was an M4 that erupted beyond the east limb at 18/10:11 UT and was thought to have originated from former Region 486.

On November 20, 2003, the geomagnetic field fluctuated between quiet and severe storm levels. There was a geomagnetic shock and a CME shock at SOHO/MTOF during 20/07:40 UT and 08:05 UT. An extremely strong (55 nT) southern component of the interplanetary magnetic field triggered geomagnetic storming in the late afternoon and evening hours. Magnetopause crossings were observed at 13:01 UT for GOES 12 and 16:28 UT for GOES 10. The M9 flare generated higher 10 MeV proton levels in geosynchronous orbit, although this activity did not surpass event thresholds.

4.1.6 The CME of November 4, 2004

A massive flare (M5/sn) with a Type IV spectral radio sweep and a Type II sweep with an estimated shock velocity of 1053 km/sec occurred at 04/23:09 UT in region 696 (N09E06) and at 04/2229Z, another flare event of class M2/1n occurred. Both these flares produced a complex partial halo CME (initial speed ~1055 km/s) and the ability to become geoeffective. Only the eastern edge of the shock generated by this CME reached Earth after roughly 66 hours. If the

accompanying shock had been Earth-directed, it would have reached in 15 hours. At 05/11:30 UT, Region 696 also produced an M4/1f. While the delta magnetic structure remains intact, the sunspot area and magnetic complexity in this region continue to grow.

On November 7th, the geomagnetic field was quiet to a major storm. At 15:55 UT, a shock arrived at ACE (Advanced Composition Explorer), causing major storming (Dst = -374) in Earth's magnetic field to begin at 16:08 UT. At 17:55 UT, another shock passage was observed at ACE, resulting in a 41nT sudden impulse at 18:31 UT, followed by minor storming. These shock passages are most likely the result of CMEs associated with the 4 November flare activity. At 19:10 UT, E > 10 MeV proton flux crossed 10 pfu and ended the period at 72 pfu. The proton flux was > 100 MeV but did not exceed the 1 pfu threshold.

Table 2 also shows that four of the six events were associated with X-class flares. In the final two occurrences, the source active region did not have any solar features that were significant enough to generate the severe storms on November 20, 2003, and November 7, 2004. This is distinct from the other super-storms (Dst 300 nT) of solar cycle 23. As a result, these phenomena are crucial in terms of space weather prediction, necessitating detailed research of the causes that contribute to them.

Table 2. List of geo effective coronal mass ejections with associated geomagnetic storms (Dst ≤ -300)

S. No.	CME date & Time (UT)	Initial speed of CME (km/s)	Travel time (hours)	Associated flare class	Storm date & Time (UT)	Dst (nT)
1	14-07-2000 10:54	1674	27.71	X5/3b	15-07-2000 14:37	-301
2	28-03-2001 12:50	519	60.03	X1/1n	31-03-2001 00:52	-387
3	2003/10/28 11:30	2459	18.68	X17/4b	2003/10/29 06:11	-353
4	2003/10/29 20:54	2029	19.48	X10/2b	2003/10/30 16:19	-383
5	2003/11/18 08:50	1660	47.21	M3/2n	2003/11/20 08:03	-422
6	2004/11/04 23:30	1055	66.95	M5/1f	2004/11/07 18:27	-374

5. RESULTS AND DISCUSSION

The morphology of the CMEs detected by the SOHO coronagraph (LASCO) consists of an occulting disc for shielding the bright light from the solar photosphere so that the indistinct coronal ejections can be observed (Brueckner et al. 1995). The classification of LASCO CMEs into six morphological categories gives an illustrative idea about the types of CMEs (Vourlidas et al. 2013, 2017; Hu et al. 2016). According to the morphological study, there are mainly three types of CMEs. The first one is the flux-rope (also known as 3-part CMEs with a circular front, a cavity, and a bright cone), the second is the halo CMEs and the third one is described as streamer blowout (narrow and different from others). The electrons contained in the photospheric light scatter and produce a bright structure due to Thomson scattering (Kilpua et al. 2013; Manchester et al. 2014; Cremades et al. 2020).

Typically, the apparent latitude of a CME is determined from the position angle of its projected angular centroid (Domingo et al. 1995). There are systematic variations in latitudes with the solar cycles (Brueckner et al. 1995; Gopalswamy et al. 2010; Cremades et al. 2020). Around the solar minima, the CMEs tend to occur at lower latitudes, while during maxima the apparent latitude increases. The magnetic loop on the hemispheres of the Sun exhibits different activity patterns and is responsible for North-South asymmetry as represented in Fig. 1 (Gopalswamy et al. 2003; Bisoi et al. 2014). This asymmetry may be associated with the variations in magnetic activity of the Sun and solar dynamo (Krivodubskij 2005; Brun et al. 2015; Harrison et al. 2018).

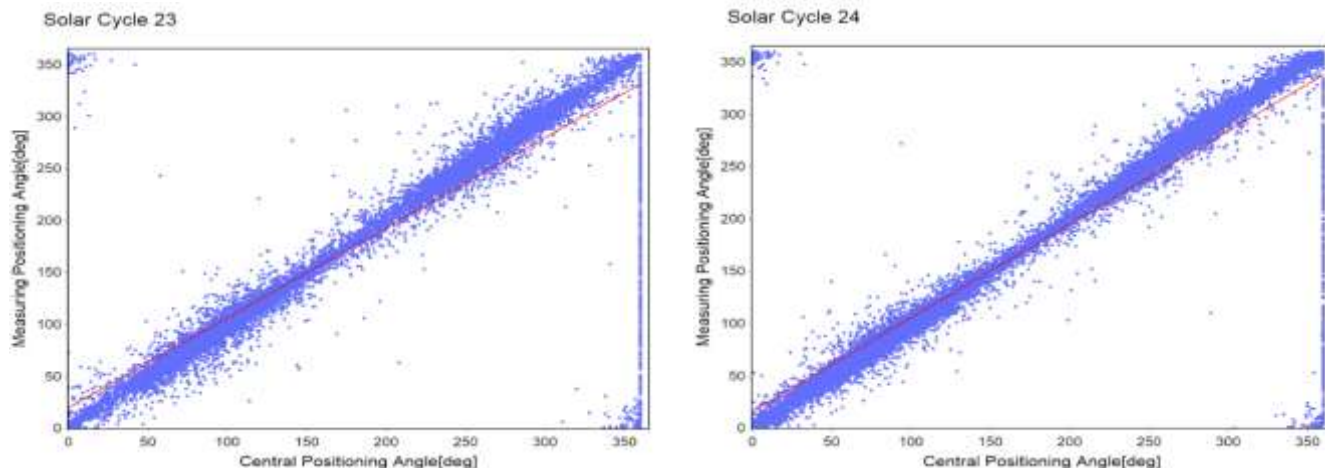


Figure. 3. Scatter plots of central positioning angle (CPA) and measuring positioning angle (MPA) of CMEs observed during solar cycles 23 and 24. The red line shows the regression line.

We have analyzed the central positioning angle (CPA) and measurement positioning angle (MPA) of CMEs observed during solar cycles 23 and 24. Fig. 3 has shown the scatter plot of the central positioning angle (CPA) and the measurement positioning angle (MPA) for solar cycles 23 and 24. Here we can infer that the Pearson's correlation coefficient (r) of CPA and MPA is relatively high in both cycles ($r = 0.88$ in solar cycle 23 and $r = 0.906$ in solar cycle 24) and correlation is statistically significant at 0.05 level with $p = 0$ in both the cycles. The linear regression of CPA and MPA (measured in degrees) gives the following equations for both solar cycles:

For solar cycle 23:

$$\text{MPA} = 0.866 (\text{CPA} + 22.75) \quad (1)$$

For solar cycle 24:

$$\text{MPA} = 0.893 (\text{CPA} + 18.07) \quad (2)$$

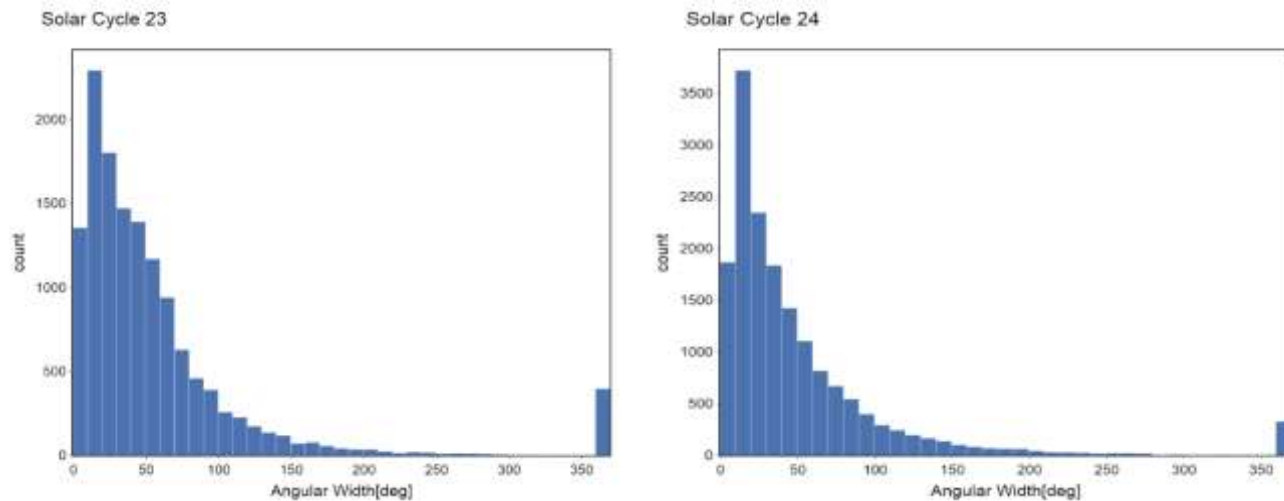


Figure 4. Histogram plot of angular width for solar cycle 23 and solar cycle 24 binned at size ($n=50$).

CPA and MPA have the same value most of the time, but their values are distinct for halo CMEs and non-radial propagating CMEs. The originating CMEs that are close to the erupting limb provide the true angular width (Hoeksema 1995; Gopalswamy et al. 2010). It is calculated as the expansion of CMEs arising from the solar surface in the sky plane and geometrical as well as projection also play a crucial role. After ejection, as the CME extends, the angular width continues to increase by the distance (Mäkelä et al. 2016; Sachdeva et al. 2017; Harrison et al. 2018). Fig. 4 shows a histogram for the apparent width (W) for all CMEs ranging from 0° to 360° for solar cycles 23 and 24 with bin size ($n=50$). The mean angular width for solar cycle 23 is $\sim 57^{\circ}$ with the median value of $\sim 39^{\circ}$ and for solar cycle 24 the mean value is $\sim 51^{\circ}$ with the median value of $\sim 31^{\circ}$. As is the fact that the CMEs having angular width 360° are known as halo CMEs (Howard et al. 1982; Shanmugaraju et al. 2015), and it appears to be brighter and bigger surrounding the occulting disk in the sky plane projection and expand rapidly around the occulting disk. During solar cycle 23, halo CMEs constitute about $\sim 2.90\%$ of all CMEs, and during solar cycle 24, halo CMEs constitute $\sim 1.95\%$. The scattered value at 360° is of halo CMEs which play an important part in Solar activities. The ordinary least square fitting is applied to find the dependency relationship between angular width and linear speed and their variation in both cycles is presented in Fig. 5. For solar cycle 23, the Pearson's correlation coefficient (r) is ~ 0.42 and is ~ 0.43 for solar cycle 24 which shows a positive and moderate correlation. Here, the two-tailed test of significance is used and correlation is significant at 0.05 level with $p = 0$ in both the cycles. Thus, the linear regression gives the following equations:

For solar cycle 23:

$$V = 1.75 (W + 184.73) \quad (3)$$

For solar cycle 24:

$$V = 1.42 (W + 187.27) \quad (4)$$

where V is the linear speed in km/s and W is the angular width in degrees.

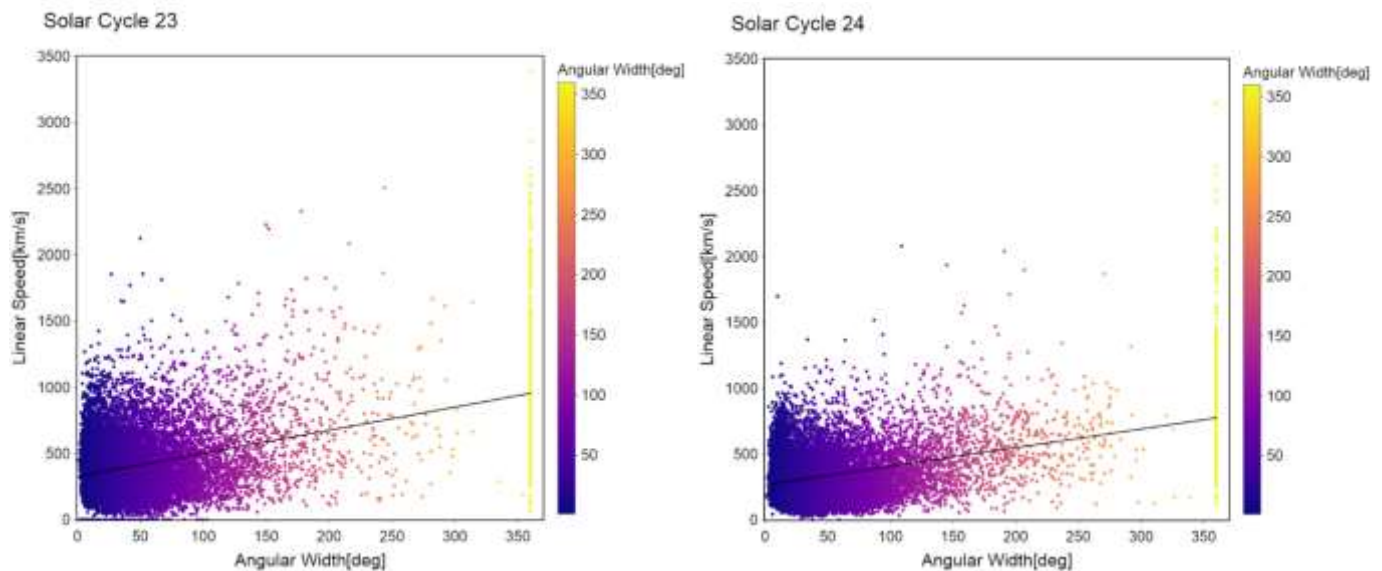


Figure. 5. Scatter plots of angular width with linear speed of CMEs for solar cycles 23 and 24. The regression line shows a positive slope and moderate correlation between angular width and linear speed.

The Kinematical properties of CMEs include linear speed, second-order initial and final speed, the second-order linear speed at a particular field of view (FOV) of coronagraphs (20R in SOHO LASCO), and acceleration (Howard & Vourlidis 2018). CMEs tend to have an initial rise duration of possibly high acceleration and subsequent constant-speed cruising phase with another possible low acceleration or deceleration in their continued expansion through the heliosphere, which implies that when their initial acceleration is low, CMEs are either 'gradual' or 'impulsive' when they are high (Harrison et al. 2018). Statistical analysis of broad data groups shows that slow CMEs originate from prominence lift-offs or streamer blow-outs and accelerate to solar wind speed, whereas fast CMEs tend to arise from flares and active regions and slow down to solar wind speed (Gopalswamy et al. 2001; Moon et al. 2002; Gonzalez-Esparza et al. 2003; Webb & Howard 2012).

For Solar Cycle 23 and 24

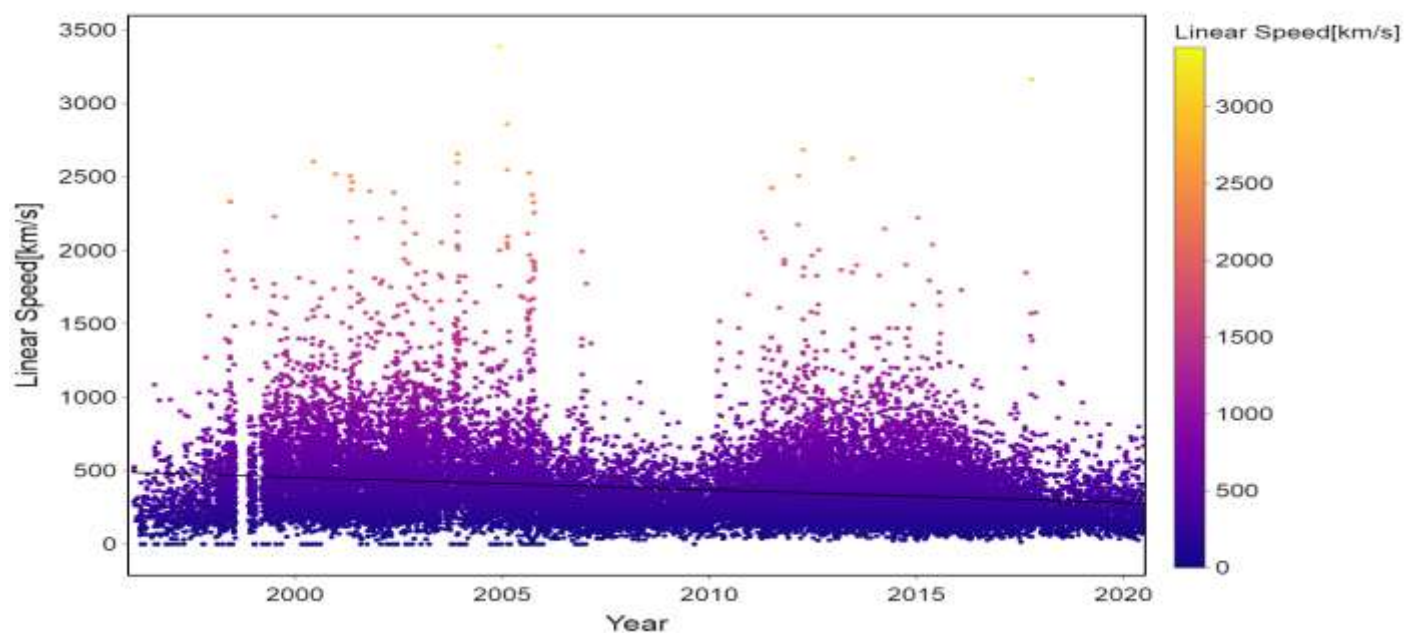


Figure. 6. Scatter plot of CMEs linear speed for both cycles 23 and 24. The regression line indicates the declining trend.

The speed of the CMEs ranges from the rest of the time within a few solar radii. The straight-line plot of the height-time measurements gives an interpretation of the mean speed within the coronagraph field of view. The mean speed measured from the plot is identical to the actual speed of the CMEs and is not near to the solar surface rather propagating in the sky plane. (Gopalswamy et. al 2009; Barlyaeva et al. 2018). Fig. 6 displays the scatter plot of time-linear speed for all CMEs in solar cycles 23 and 24 and shows the rise and decrease in linear speed between 1996-2008 (solar cycle 23) and 2008-2020 (solar cycle 24). The maximum linear speed observed in the solar cycle 23 is ~3387 km/s and the solar cycle 24 is ~3163 km/s, which also underpins the decreasing pattern of solar activity in the coming solar cycles. The fitted solid line displays the ordinary least square fit of the predicted linear speed values, with a negative slope suggesting a decline in the projected linear speed of the solar cycle 24. This means that while the number of eruptions in the solar cycle 24 is higher relative to the solar cycle 23, the extension of CMEs to the heliosphere is lower, and the eruptions in the solar cycle 24 are less energetic than the eruptions in cycle 23.

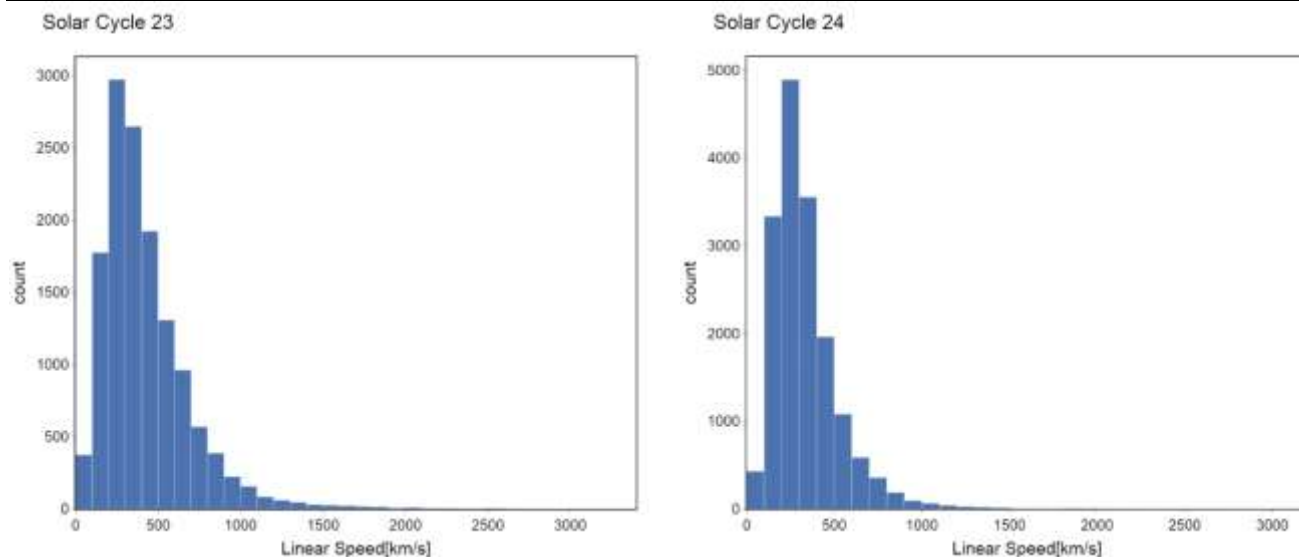


Figure. 7. Histogram plot (bin size = 50) for CMEs linear speed for solar cycle 23 and solar cycle 24.

Fig. 7 illustrates a histogram of linear speed with bin size (n=50) for all CMEs in the solar cycles 23 and 24. The mean linear speed and the median value for the solar cycle 23 is ~425 km/s and ~360 km/s, for cycle 24 these values are ~337.36 km/s and ~292 km/s. Fig. 8 has presented a scatter graph (time-linear speed) of second-order linear speed at 20R. CMEs ranging up to 20R hold energy and mass which are expected to induce a difference in the Earth's magnetic field. The kinematic properties of CMEs can be described as a first-order linear fit for height-time measurements, but this is limited for certain CMEs only, other CMEs can better be described as a second-order polynomial fit (acceleration). The resulting acceleration typically depends on the original speed (or its square) within the coronagraph field of view (Gopalswamy et al. 2001). The acceleration of the protruding CMEs is not constant due to the various forces (gravity, drag) acting on the CMEs (Vršnak et al. 2004; Howard & Vourlidas 2018).

For Solar Cycle 23 and 24

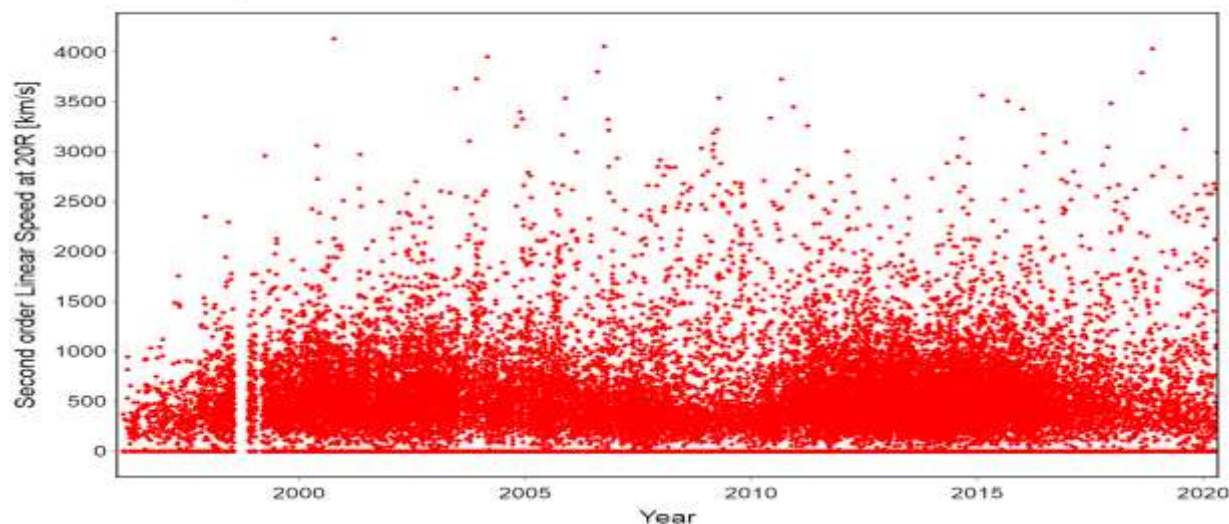


Figure. 8. Scatter plot for the second-order linear speed 20R of all CMEs occurred in solar cycles 23 and 24.

Observations and statistics have shown that CMEs moving quicker than the slow solar wind decelerate, whereas the slower ones accelerate (Gopalswamy 2010; Manchester et al. 2017). Fig. 9 shows a scatter plot and linear regression between the CMEs' linear speed and acceleration giving the equations (5) and (6).

For solar cycle 23:

$$A = - 0.01134 (V - 518.85) \dots\dots (5)$$

For solar cycle 24:

$$A = - 0.00255 (V - 2411.11) \dots\dots (6)$$

where A represents the acceleration (m/s²) and V is the linear speed (km/s). The Pearson's correlation coefficients obtained are ~ -0.071 and ~ -0.011 for solar cycles 23 and 24 respectively which indicates that acceleration and speed are showing a negative and extremely weak correlation.

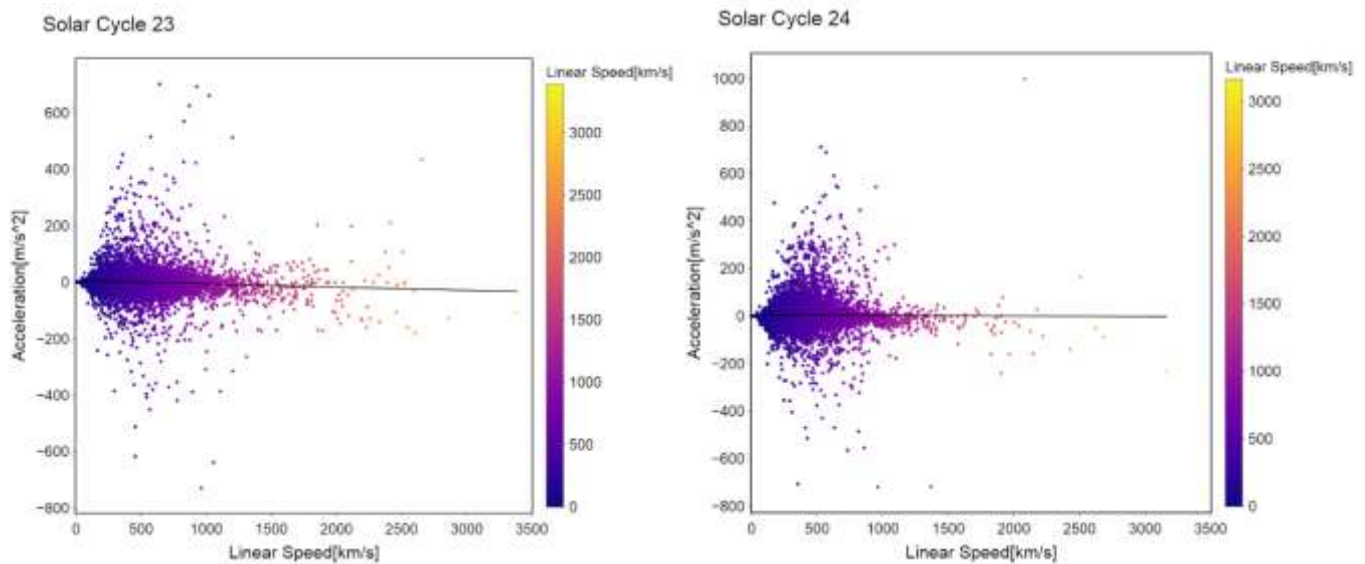


Figure 9. Scatter plots of CMEs linear speed and acceleration for solar cycle 23 and solar cycle 24. The regression line indicates a weak correlation between linear speed and acceleration.

The two-tailed test of significance is used for the analysis and correlation is significant at 0.05 level with p -value = 0 in both the cycles. From the equation, therefore, it should be concluded that these equations can be used as an empirical relationship between linear speed and acceleration of CMEs.

Fig. 10 shows the histogram plot of acceleration (bin size = 50) for all CMEs during cycles 23 and 24, the mean and median value of acceleration for the solar cycle 23 is about $\sim 1.064 \text{ m/s}^2$ and $\sim 0.2 \text{ m/s}^2$ and for solar cycle 24 is about $\sim 4.62 \text{ m/s}^2$ and $\sim 2.5 \text{ m/s}^2$.

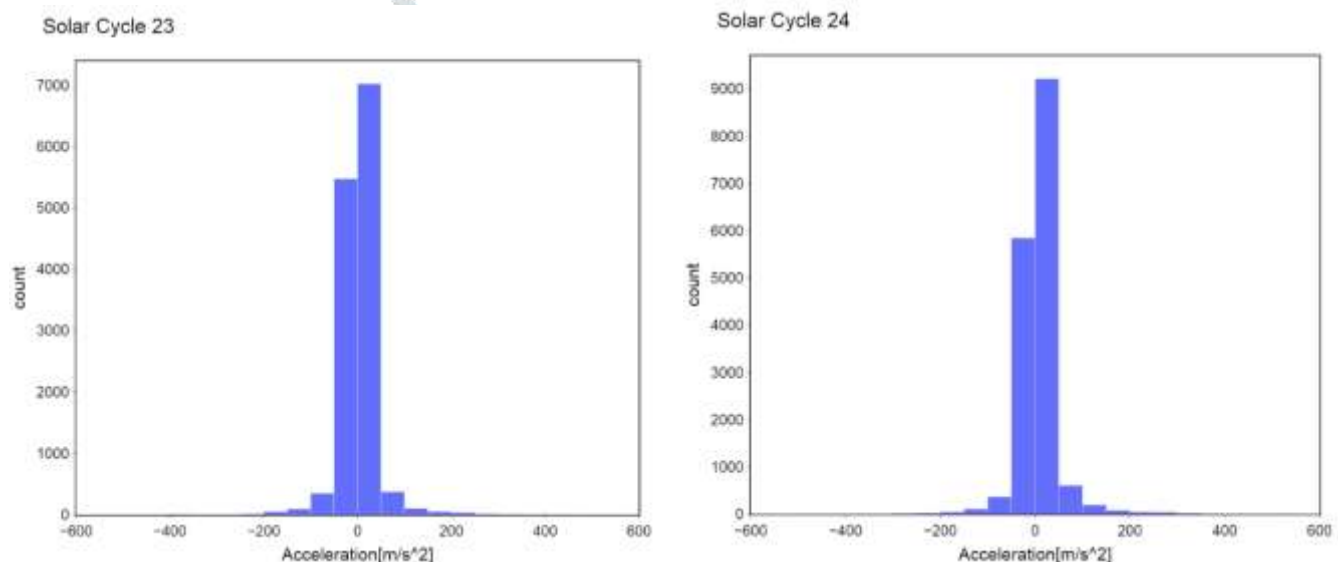


Figure 10. Histogram plot binned at size of $n=50$ for acceleration of all CMEs observed during solar cycle 23 and solar cycle 24.

The mass ejected by the CMEs ranges from 10^{12} - 10^{16} grams (Gopalswamy 2010). Fig. 11 shows a line graph of total mass ejected for all CMEs during cycles 23 and 24. The CME mass is determined by measuring the number of electrons required in the sky plane to achieve the observed CME brightness (Gopalswamy 2010; Howard & Vourlidas 2018). The maximum value of mass ejected during solar cycle 23 (13640 CMEs) is $\sim 2 \times 10^{17}$ gram with a mean value of $\sim 1.18 \times 10^{15}$ gram and a median $\sim 1.5 \times 10^{14}$ gram. The maximum mass ejected during cycle 24 (16680 CMEs) is $\sim 1.2 \times 10^{17}$ gram with a mean value $\sim 8.24 \times 10^{14}$ gram and median $\sim 7.1 \times 10^{13}$ gram. Fig. 12 shows a histogram plot of logarithm of total mass ejected during solar cycles 23 and 24 in which difference in the total mass ejected in both cycles can be seen. CMEs with a larger angular width have more mass (Gopalswamy et al. 2005). Some of the data for which the value of mass ejected is not given in the SOHO LASCO catalog is not considered in the statistical analysis.

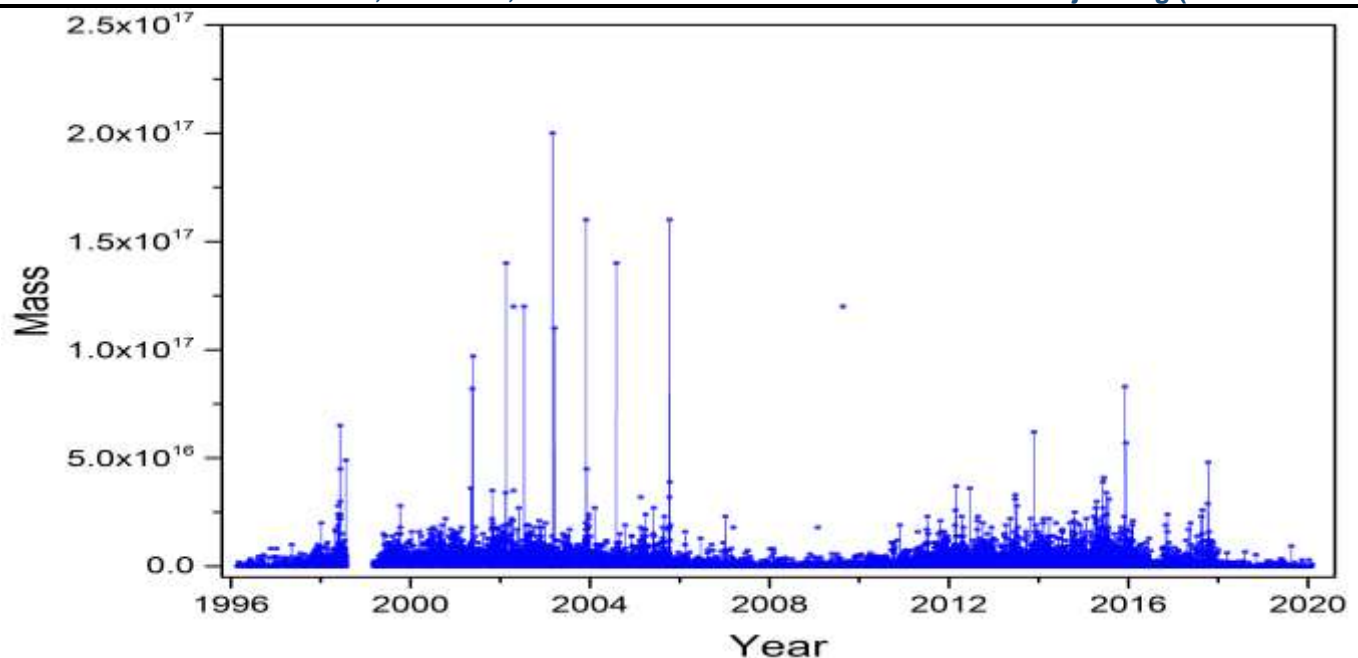


Figure. 11. Line plot of total mass ejected during solar cycles 23 & 24 (1996 - 2020).

The relationship between CME speed and width reveals that the CMEs with wider angular width are usually faster and more massive (Gopalswamy et al. 2009b; Howard & Vourlidas 2018), implying that the CMEs with higher speed and width contain higher kinetic energy with them (Gopalswamy 2010). So, the computation of kinetic energy can be done using linear speed and mass (Vourlidas et al. 2010; Barlyaeva et al. 2018). The kinetic energy of mass ejected from CMEs ranges between 10^{26} erg - 10^{33} erg. Fig. 13 shows histogram plot of logarithm of total kinetic energy for all CMEs during solar cycles 23 and 24. The maximum value of kinetic energy during solar cycle 23 (13640 CMEs) is $\sim 4.2 \times 10^{33}$ erg with the mean value of $\sim 4.23 \times 10^{30}$ erg and median $\sim 5.6 \times 10^{28}$ erg. The maximum kinetic energy during solar cycle 24 (16680 CMEs) is $\sim 1.2 \times 10^{33}$ erg with a mean value of $\sim 2.23 \times 10^{30}$ erg and median $\sim 1.7 \times 10^{28}$ erg. Some of the missing kinetic energy data are not considered in the analysis because of the elimination of faint CMEs.

One of the early indicators of a weak solar cycle 24 was the significantly reduced number of large geomagnetic storms ($Dst \leq -100$ nT) (Kilpua et al. 2014). Fig. 14 depicts a time series plot of the Dst index, revealing that the frequency and amplitude of storms in cycle 24 are the lowest in the space age (cycles 19 to 24). Storms with $Dst < -200$ nT occurred in every cycle since 1957, except for cycle 24, when storms never exceeded 140 nT. Several historical storms may be identified in the Fig., including recent ones on 14 March 1989 with $Dst = -589$ nT and 20 November 2003 with $Dst = -422$ nT.

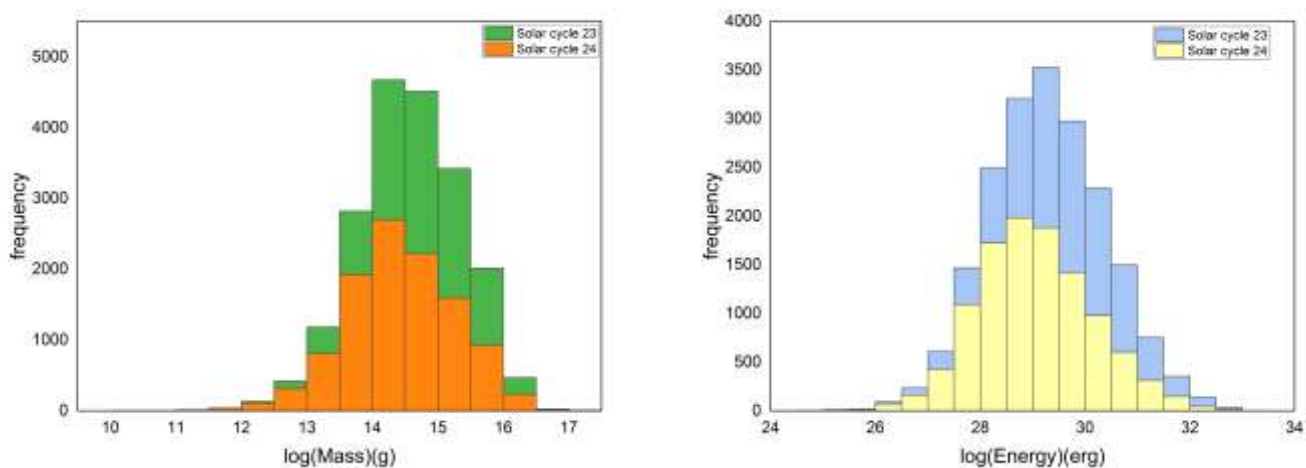


Figure. 12,13. Histogram plot of log(mass)(g) ejected and log (kinetic energy) (erg) during the solar cycles 23 & 24.

In terms of geomagnetic activity, the solar cycle 24 (SC24) has been criticized repeatedly. Only a few days of severe geomagnetic conditions, and no exceptionally strong geomagnetic storms, have rendered SC24 a significant let down in terms of the amount of geomagnetic activity. In the last few years, observations and recordings have only confirmed this conclusion. When it comes to other parameters, Julius Bartels' Kp-index, introduced in 1949 and extended back to 1932, is the most commonly used (Elliot et al. 2013). Using magnetic records from 13 sub-auroral observatories, this 3-hour range index was calculated for a 3-hour period. It is commonly written as 0o, 0+, 1-, 1o, 1+, 2-, ..., 8+, 9o. They are all expressed in complete Fig.s, including the estimated Kp and the local K indices (0, 1, ..., 8, 9). Low numbers, such as "0" or "1," indicate quiet geomagnetic circumstances, but high values, such as "8" or "9," indicate severe and extremely severe geomagnetic conditions, respectively (Olsen & Stolle 2017). It is important to note that the scale is open-ended, which means that no matter how high the geomagnetic variation is, Kp will never surpass 9.

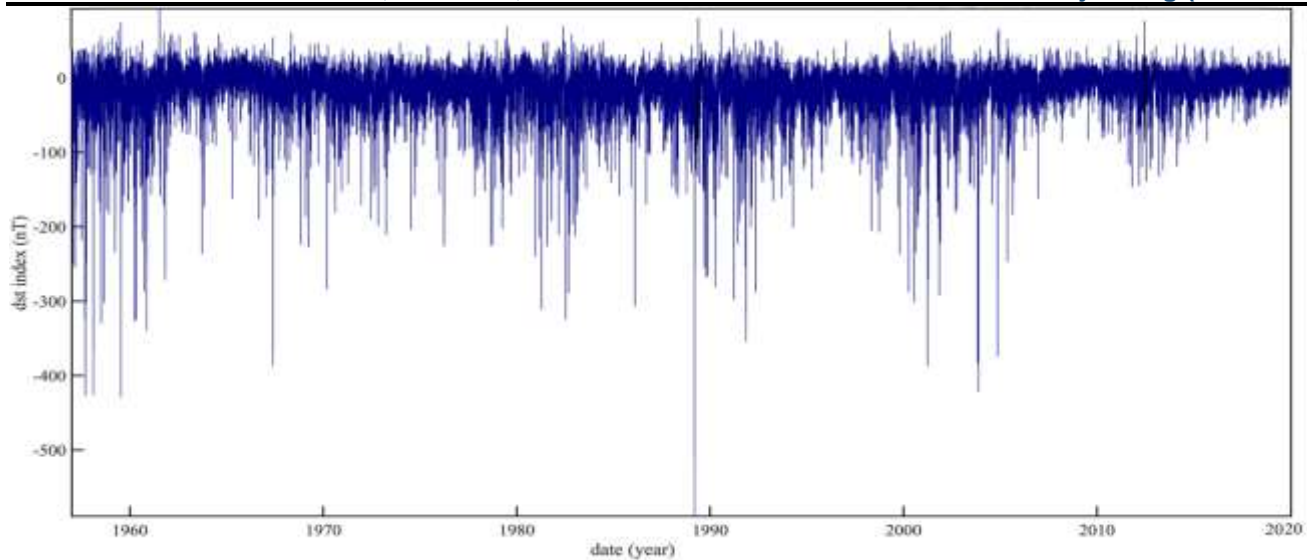


Figure. 14. The Dst index as a function of time from 1957 to 2020.

A brief scan of the final Kp indices for geomagnetism as archived at the Kyoto World Data Centre (WDC) reveals that SC24 is a true underachiever. Not only has there not been a single day of significant geomagnetic storming, but SC24 has also recorded a lot fewer storming days (Kp 5) and a lot more "quiet" days (Kp 2) than the prior 7 solar cycles on average (SC17-23). Fig. 15 depicts this, with the blue-dashed lines representing the standard deviation. SC24 is overpopulated with quiet days compared to the average of the previous four solar cycles (SC20-23), but it lacks a high number of storm days, with not a single "very intense" day. Therefore, SC24 was an underperformer in terms of geomagnetic activity.

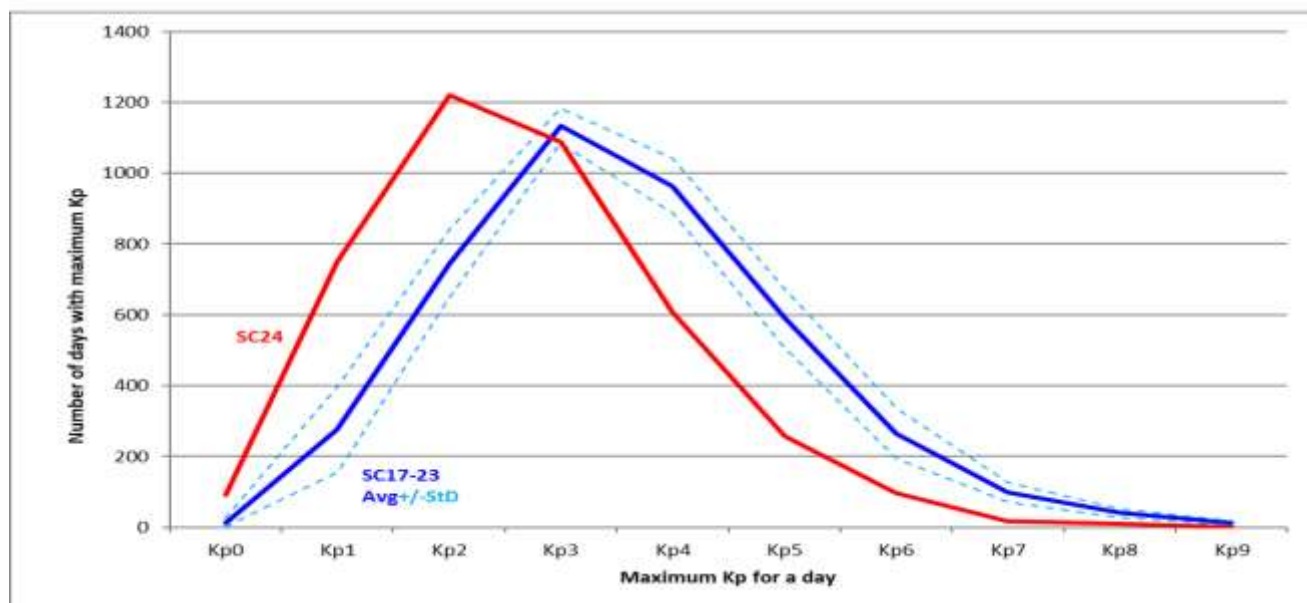


Figure. 15. Number of days with maximum Kp index values vs maximum Kp for a day.

M3.9 class flare on 20 November 2003 generated the most powerful storm (Dst > -472nT) even though high-speed CMEs and X-class flare activity in vast active zones were responsible for the majority of superstorms. CMEs with the modest plane of sky speeds (~1660 km/s) were the genesis of this geomagnetic storm, which presented a major challenge for space weather forecasts. Coronal Mass Ejections have been studied extensively, and it has been determined they are the result of a combination of factors including a high interplanetary magnetic field (~52 nT), a strong southward component of the interplanetary magnetic field (~ -56nT), and an inclination that ensured that the magnetic cloud was strongly reconnected to the earth's magnetosphere during the geomagnetic storm of November 18, 2003, CME by Gopalswamy et al. (2005a) and Yurchyshyn et al. (2005). The CMEs of November 4, 2004, most likely interacted with shocks and a magnetic cloud (MC), which consisted of two shocks and an MC. Both periods had long intervals of high IMF (59 nT) and strong southward interplanetary magnetic field (less than -50 nT) (IMF). The solar wind continued to be fast between these two distinct structures, while other solar wind parameters and the IMF became relatively quiet. As a result, lower-intensity X-ray flares can cause stronger storms, as observed during our study period. It follows from this that geomagnetic activity is not correctly predicted by the strength of the flare in optical or X-ray light. There is a link between a C- and M-class flare and severe storms (Dst -100 nT).

For the period 1996 to 2020, we analyzed all 91 geo-effectiveness of CMEs that generated severe geomagnetic storms (DST index less than -100 nT). According to recent studies by LASCO, CMEs display certain different features independent of their direction of motion. For all geoeffective CMEs recorded between 1996 and 2020, the starting speeds vary from 500 to 2500 km/h in the FOV of LASCO-C2. Pearson's coefficient of 0.66 was shown to be negatively correlated with geomagnetic activity and therefore, the initial speed of the CME and the storm's DST strength are moderately correlated (Fig. 16). Fig. 17 illustrates that the severe geomagnetic storms are connected with solar flares of class X and M that originated from the central-northern area, and these flares came from old active regions. X17/4b and X10/2b were the two most powerful flares of solar cycle 23. They were both

produced by Region 486 located in southern part near the equator. M class flares were found to be concentrated in the central northern region of the sun near the equator, whereas C class flares erupted from the western and eastern limbs (Fig. 17).

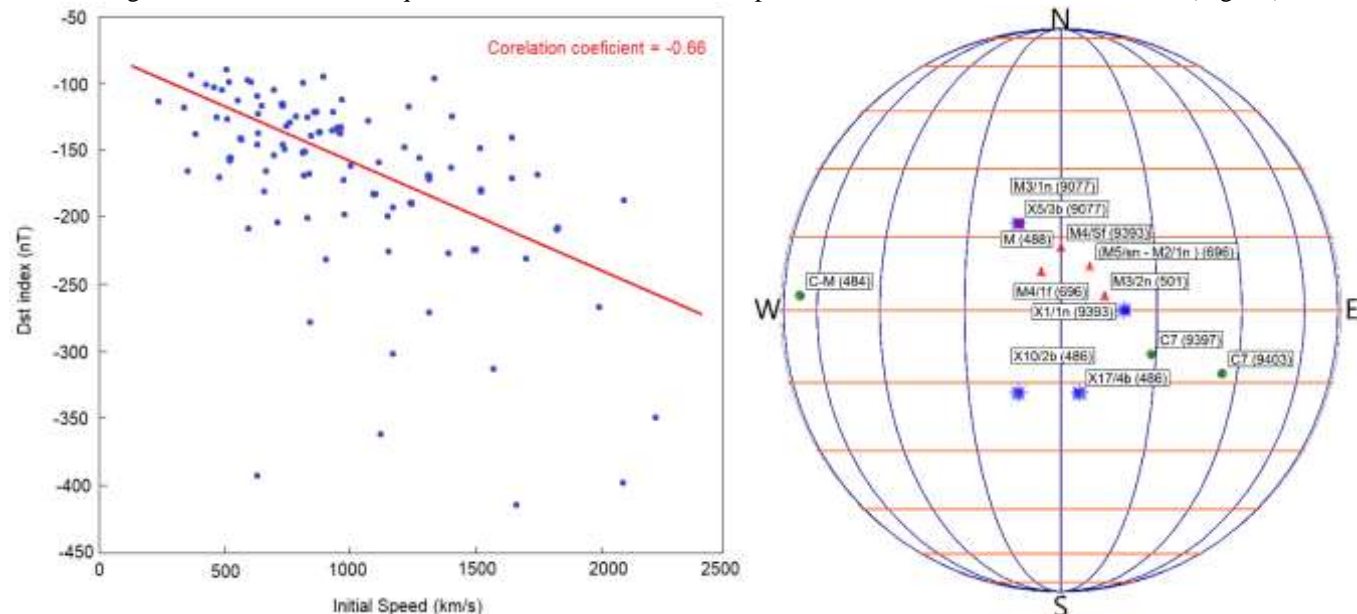


Figure. 16 & 17. The geomagnetic storm intensity plotted against the initial speeds of CMEs shows a good association and Location of intense solar flares (X, M, C class used in case study of extreme geomagnetic storm) as a function of solar longitude (in degrees) and active regions associated with the flares.

Table 1. Comparative chart of sunspot numbers and the observed properties of coronal mass ejections (CMEs) for solar cycles 23 and 24.

Comparison of Observational Properties of CMEs in Solar Cycle 23 and 24			
Observational Properties	Solar Cycle 23 ^a	Solar Cycle 24 ^b	Ratio ^c
Total Number of CMEs	13640	16680	1.223
Mean Total SSN	78.82	48.15	0.611
Mean North SSN	36.97	25.11	0.679
Mean South SSN	41.84	23.03	0.551
Mean Angular Width	57°	51°	0.895
Median Angular Width	39°	31°	0.795
Mean Linear Speed	425 km/s	337.46 km/s	0.794
Maximum Linear Speed	3387 km/s	3163 km/s	0.934
Mean Acceleration	1.064 m/s ²	5.29 m/s ²	4.972
Mean Mass Ejected	1.18 × 10 ¹⁵ gram	8.24 × 10 ¹⁴ gram	0.698
Median Mass Ejected	1.5 × 10 ¹⁴ gram	7.1 × 10 ¹³ gram	0.473
Maximum Mass Ejected	2 × 10 ¹⁷ gram	1.2 × 10 ¹⁷ gram	0.600
Mean Kinetic Energy	4.23 × 10 ³⁰ erg	2.23 × 10 ³⁰ gram	0.527
Median Kinetic Energy	5.6 × 10 ²⁸ erg	1.7 × 10 ²⁸ erg	0.304
Maximum Kinetic Energy	4.2 × 10 ³³ erg	1.2 × 10 ³³ erg	0.286
Number of Halo CMEs	396	326	0.823
Percentage of Halo CMEs	2.90%	1.95%	0.672
Mean Linear Speed of Halo CMEs	1040.11 km/s	904.77 km/s	0.869
<i>a. From Jan 1996 - June 2008</i>			
<i>b. From July 2008 - June 2020</i>			
<i>c. Ratio of Solar Cycle 24 to Solar Cycle 23</i>			

5. CONCLUSIONS

As part of the present work, we have studied several observational characteristics of CMEs during solar cycles 23 and 24 from 1996 to 2020. We have collated various aspects of CMEs about the overall solar activity represented by the total and hemispherical sunspot numbers. The following are some of the most important conclusions from this statistical analysis:

- We depicted differences in the sunspot numbers in the north and south hemispheres in the solar cycles 23 and 24 which prominently shows the existence of N-S asymmetry.

- A higher number of weak and low energetic CMEs prevailed in the solar cycle 24 than in cycle 23. This difference in the rate of CMEs and solar activity means that the rate of ejection does not depend too much on the number of sunspots.
- The histogram plots of angular width for both the cycles have shown that the mean and median values of angular width in solar cycle 23 were more than in solar cycle 24.
- The CME linear speed-time graph with a negative slope shows the significant decrease in the linear speed during solar cycle 24 which has concluded about the weak solar activity during solar cycle 24.
- Pearson's Correlation coefficient of angular width to the linear speed of CMEs revealed positive and moderate correlation, while acceleration and linear speed were negative and weakly correlated with each other.
- Other observational properties of CMEs, such as the mass expelled and kinetic energy of CMEs, also demonstrated a reduced value in the solar cycle 24.
- Geomagnetic activity during solar cycle 24 was very low as compared to its three precursors.
- In our case study of geomagnetic storms, we discovered that the majority of the intense solar flares (mostly X and M class) causing the extreme geomagnetic events originate from the former active regions in the central north hemispherical region near the equator, while low M and C class are near the eastern and western limbs.
- The strength of the flare in optical or X-ray images does not accurately predict the intensity of the geomagnetic activity that would occur. However, even C and M class flares can be accompanied by severe storms ($Dst > -100$ nT).
- The initial speed of CMEs and geomagnetic activity was found to have a moderate and negative Pearson's correlation coefficient of 0.66. This correlation suggests that the prediction of geo-effectiveness is associated with the initial speed of halo CMEs.

6. ACKNOWLEDGMENT

We acknowledge the use of data obtained from the websites [https://cdaw.gsfc.nasa.gov/CME list/](https://cdaw.gsfc.nasa.gov/CME_list/), Silso World Data Center, and Japan World Data Center. PS is grateful for the fellowships provided by the University Grants Commission (UGC).

7. CONFLICT OF INTEREST: THE AUTHORS DECLARE THAT THEY HAVE NO CONFLICT OF INTEREST.

References

- [1] Adam, P., Mrotzek, N., Vourlidas, A., Bothmer, V., Savani, N. 2019, *A&A*, 623, A139
- [2] Anastasiadis, A., Lario, D., Papaioannou, A., Kouloumvakos, A., Vourlidas, A. 2019, *Phil. Trans. R. Soc. A*, 377, 20180100
- [3] Ballester, J.L., Oliver R., Carbonell M. 2005, *A&A*, 431, L5-L8
- [4] Barlyaeva, T., Wojak, J., Lamy, P., Boclet, B., Toth, I. 2018, *J. Atmos. Sol. Terr. Phys.* 177, 12–28
- [5] Bisoi, S.K., Janardhan, P., Chakrabarty, D., Ananthakrishnan, S., Divekar, A. 2014, *Sol. Phys.*, 289, 41–61
- [6] Brueckner, G.E., Howard, R.A., Koomen, M.J., et al., 1995, *Sol. Phys.*, 162, 357
- [7] Brun, A.S., García, R.A., Houdek, G., Nandy, D., Pinsonneault, M., 2015, *Space Sci. Rev.*, 196, 303–356
- [8] Cremades, H., Iglesias, F.A., Merenda, L.A. 2020, *A&A*, 635, A100
- [9] Domingo, V., Fleck, B., Poland, A.I. 1995, *Sol. Phys.*, 162, 01-37
- [10] Echer, E., Gonzalez, W. D., & Tsurutani, B. T. 2008, *Geophysical Research Letters*, 35(6)
- [11] Elliott, H. A., Jahn, J. M., & McComas, D. J., et al. 2013, *Space Weather*, 11(6), 339-349
- [12] Fainshtein, V.G., Popova, T.E., Kashapova, L.K. 2012, *Geomagn. Aeron.*, 52, 1075
- [13] Giacalone, J., Mitchell, D.G., Allen, R.C., et al. 2020, *Astrophys. J.*, 246, 29
- [14] GIAMINI, S.A., JIGGENS, P., ANASTASIADIS, A., ET AL. 2020, *J. SPACE WEATHER SPACE CLIM*, 10, 01-16
- [15] González-Esparza, J.A., Lara, A., Pérez-Tijerina, E., Santillán, A., Gopalswamy, N. 2003, *J. Geophys. Res.*, 108, 1039
- [16] Gopalswamy, N., Lara, A., Yashiro, S., Kaiser, M., Howard, R.A. 2001, *J. Geophys. Res.*, 106, 29207
- [17] Gopalswamy, N., Lara, A., Yashiro, S., Howard, R.A. 2003, *ApJ Lett.*, 598, 63–66
- [18] Gopalswamy, N., Aguilar-Rodriguez, E., Yashiro, S. et al. 2005, *J. Geophys. Res.*, 110, A12S07
- [19] Gopalswamy, N. 2008, *Journal of Atmospheric and Solar-Terrestrial Physics*, 70(17), 2078-2100
- [20] Gopalswamy, N., Akiyama, S., Yashiro, S., Michalek, G., & Lepping, R. P. 2008, *Journal of Atmospheric and Solar-Terrestrial Physics*, 70(2-4), 245-253
- [21] Gopalswamy, N., Dal Lago, A., Yashiro, S., and Akiyama, S. 2009, *Central European Astrophysical Bulletin*, 33, 115
- [22] Gopalswamy, N. 2009, *Proceedings of the International Astronomical Union*, 5(S264), 326-335
- [23] Gopalswamy, N., Yashiro, S., Michalek, G. et al. 2009, 104, 295–313
- [24] Gopalswamy, N., Akiyama, S., Yashiro, S., Mäkelä, P. 2010, *Astrophysics and Space Science Proceedings*. Springer Berlin Heidelberg. pp 289-307
- [25] Gopalswamy, N., Xie, H., Akiyama, S., Mäkelä, P., Yashiro, S., Michalek, G. 2015, *Astrophys J*, 804, L23
- [26] Green, L.M., Török, T., Vršnak, B. et al. 2018, *Space Sci. Rev.*, 214, 46
- [27] Harrison, R.A., Davies, J.A., Barnes, D., Byrne, J.P., Perry, C.H., et al, 2018, *Sol. Phys.*, 293, 77
- [28] Hoeksema, J.T. 1995, *Space Sci. Rev.*, 72, 137
- [29] Howard R.A., Vourlidas A. 2018, *Sol. Phys.*, 293, 55
- [30] Howard, R.A., Michels, D.J., Sheeley Jr, N. R., Koomen, M. J. 1982, *ApJ*, 263, L101
- [31] Hu, H., Liu, Y.D., Wang, R., Möstl, C., Yang, Z. 2016, *ApJ*, 829, 97
- [32] Jang, M., Woods, T.N., Hong, S., Choe, G.S. 2016, *ApJ*, 833, L11
- [33] Kane, R.P. 2009, *Solar Phys.*, 255, 163
- [34] Kennel, C. F., Edmiston, J. P., & Hada, T. 1985, *A tutorial review*, 34, 1-36
- [35] Kilpua, E.K.J., Isavnin, A., Vourlidas, A., Koskinen, H.E.J., Rodriguez, L. 2013, *Ann. Geophys.*, 31, 1251–1265
- [36] Kilpua, E. K. J., Luhmann, J. G., Jian, L. K., Russell, C. T., & Li, Y. 2014, *Journal of Atmospheric and Solar-Terrestrial Physics*, 107, 12-19
- [37] Kim, R.S., Cho, K.S., Moon, Y.J., et al. 2010, *J. Geophys. Res.*, 115, A12108

- [38] Krivodubskij, V.N. 2005, *Astron. Nachr.*, 326, 61–74
- [39] Lamy, P.L., Floyd, O., Quémerais, E., Boclet, B., Ferron, S. 2017, *J Geophys. Res. Space Phys.*, 122, 50–62
- [40] Lamy, P.L., Floyd, O., Boclet, B. et al. 2019, *Space Sci. Rev.*, 215, 39
- [41] Low, B.C. 2001, *J. Geophys. Res.*, 106, 25141– 25164
- [42] Mäkelä, P., Gopalswamy, N., Yashiro, S. 2016, *Space Weather*14, 368
- [43] Manchester, W. B., Gombosi, T. I., De Zeeuw, D. L. 2005, *The Astrophysical Journal*, 622(2), 1225
- [44] Manchester, W., van der Holst, B., Lavraud, B. 2014, *Plasma Phys. Control. Fusion*, 56, 01–11
- [45] Manchester, W., Kilpua, E.K.J., Liu, Y.D. et al. 2017, *Space Sci. Rev.*, 212, 1159-1219
- [46] Moon, Y.J., Choe, G.S., Wang, H., et al. 2002, *ApJ*, 581, 694
- [47] Nieves-Chinchilla, T., Szabo, A., Korreck, K.E., et al. 2020, *Astrophys. J.*, 246, 63
- [48] Olsen, N., & Stolle, C. 2017, *Space Science Reviews*, 206(1-4), 5-25
- [49] Padmanabhan, J., Bisoi, S. K., Ananthakrishnan, S., et al. 2015, *J. Geophys. Res.*, 120, 5306
- [50] Petrie, G.J.D. 2013, *Astrophys. J.*, 768, 162
- [51] Pevtsov, A.A., Canfield, R.C. 2001, *J. Geophys. Res.*, 106, 25191
- [52] Qiu, J., Yurchyshyn, V.B. 2005, *ApJ Lett.*, 634, L121
- [53] Richardson, I.G., Cane, H.V. 2004, *Geophys. Res. Lett.*, 31, L18804
- [54] Sachdeva, N., Subramanian, P., Vourlidas, A., Bothmer, V. 2017, *Sol. Phys.*, 292, 118
- [55] Sabaka, T. J., Olsen, N., & Purucker, M. E. 2004, *Geophysical Journal International*, 159(2), 521-547
- [56] Shanmugaraju, A., Bendict Lawrance, M. 2015, *Sol. Phys.*, 290, 2963-2973
- [57] Singh, A.K., Singh, R.P. 2003, *Indian J. Phys.*, 77, 611-616
- [58] Singh, A.K., Bhargawa, A. 2017, *Astrophys. Space Sci.*, 362, 199
- [59] Singh, A.K., Bhargawa, A. 2019, *Astrophys. Space Sci.*, 364, 12
- [60] Singh, A.K., Siingh, D., Singh, R.P. 2010, *Surveys in Geophysics*, 31, 581-638
- [61] Singh, A.K., Tonk, A., Singh, R. 2014, *Indian J. Physics* 88, 2711-2716
- [62] Singh, A.K., Bhargawa, A., Tonk, A. 2018, *J. Astrophysics Astronomy*, 39, 32
- [63] Srivastava, N., & Venkatakrisnan, P. 2002, *Geophysical research letters*, 29(9), 1-1
- [64] Subramanian, P., Dere, K.P. 2001, *Astrophys. J.*, 561, 372
- [65] Taktakishvili, A., Kuznetsova, M., MacNeice, P., et al. 2009, *Space Weather* 07, S03004
- [66] Verma, V.K. 1993, *Astrophys. J.*, 403, 797-800
- [67] Vourlidas, A., Balmaceda, L.A., Stenborg, G., Dal Lago, A. 2017, *ApJ*, 838, 141
- [68] Vourlidas, A., Howard, R.A., Esfandiari, E. 2010, *ApJ*, 722, 1522
- [69] Vourlidas, A., Lynch, B.J., Howard, R.A., Li, Y. 2013, *Sol. Phys.*, 284, 179–201
- [70] Vršnak, B., Ruždjak, D., Sudar, D., and Gopalswamy, N. 2004, 423, 717
- [71] Waldmeier, M. 1971, *Sol. Phys.*, 20, 332-344
- [72] Wang, Y., Colaninno, R. 2014, *ApJ*, 784, L27
- [73] Wang, Y., Zhang, J. 2008, *ApJ*, 680, 1516
- [74] Webb, D. F., & Jackson, B. V. 1990, *Journal of Geophysical Research: Space Physics*, 95(A12), 20641-20661
- [75] Webb, D.F., Howard, R.A. 1994, *J. Geophys. Res.*, 99, 4201-4220
- [76] Webb, D. F., Howard, T. A., Fry, C. D, et al. 2009, *Sol. Phys.*, 256(1), 239-267
- [77] Webb, D.F., Howard, T.A. 2012, *Sol. Phys.*, 9, 3
- [78] Werner, A.L.E., Yordanova, E., Dimmock, A.P., Temmer, M. 2019, *Space Weather*, 17, 357–369
- [79] World Data Center for Geomagnetism, Kyoto, M. Nose, T. Iyemori, M. Sugiura, T. Kamei 2015, *Geomagnetic Dst index*
- [80] Xapsos, M.A., Summers, G.P., Barth, J.L., Stassinopoulos, E.G., Burke, E.A. 1999, *IEEE Trans. Nucl. Sci.*, 46, 1481–1485
- [81] Yurchyshyn, V., Yashiro, S., Abramenko, V., Wang, H., & Gopalswamy, N. 2005, *The Astrophysical Journal*, 619(1), 599
- [82] Yurchyshyn, V., Hu, Q., Lepping, R.P., Lynch, B.J., Krall, J. 2007, *Adv. Space Res.*, 40, 1821–1826
- [83] Zhang, J., Richardson, I. G., Webb, D. F. 2007, *Journal of Geophysical Research: Space Physics*, 112(A10)
- [84] Zolotova, N.V., Ponyavin, D.I. 2014, *J. Geophys. Res.*, 119, 3281